A Multi-Fidelity Modelling approach to the Statistical Inference of the Equivalent Initial Flaw Size Distribution for Multiple-Site Damage

Llewellyn Morse [a,*], **Zahra Sharif Khodaei** [a], **M. H. Aliabadi** [a]
[a] *Department of Aeronautics, Imperial College London, South Kensington Campus, City and Guilds Building, Exhibition Road, SW7 2AZ, London, UK.*

Abstract

A new methodology for the statistical inference of the Equivalent Initial Flaw Size Distribution (EIFSD) using the Dual Boundary Element Method (DBEM) is proposed. As part of the inference, Bayesian updating is used to calibrate the EIFS based on data obtained from simulated routine inspections of a structural component from a fleet of aircraft. An incremental crack growth procedure making use of the DBEM is employed for the modelling of the simultaneous growth of cracks in the structure due to fatigue. Multi-fidelity modelling, in the form of Co-Kriging, is used to create surrogate models that act in place of the DBEM model for the expensive Monte Carlo sampling procedure required for the statistical inference of the EIFSD. The proposed methodology is applied to a numerical example featuring a long fuselage lap joint splice in presence of Multiple Site Damage (MSD). Results show that the EIFSD can be accurately estimated within 10% error with data from just 50 inspections. The employed Co-Kriging models proved to be effective substitutes for the DBEM model, providing significant reductions in the computational cost associated with the implementation of the proposed statistical inference methodology.

Keywords: Equivalent Initial Flaw Size Distribution; Fatigue crack growth; Multiple Site Damage; Multi-fidelity modelling; Dual Boundary Element Method

Abbreviations: Equivalent Initial Flaw Size Distribution (EIFSD); Multiple Site Damage (MSD); Dual Boundary Element Method (DBEM)

*Corresponding author.
E-mail addresses: llewellyn.morse12@imperial.ac.uk (L. Morse), z.sharif-khodaei@imperial.ac.uk (Z. Sharif Khodaei), m.h.aliabadi@imperial.ac.uk (M. H. Aliabadi)

1. Introduction

Fatigue is the leading cause of structural failure in aircraft, and is among the most common causes of failure in other engineering structures [1]. By better understanding the mechanics behind fatigue crack growth, the fatigue life of a structure can be more accurately estimated. The timing of inspections can therefore be more accurately determined, providing improvements in both the efficiency of maintenance and safety. Current damage tolerance specifications state that the designer should assume that the initial cracks in the structure are of a size that is the maximum that could remain undetected after the use of a non-destructive inspection (NDI) technique [2]. However, because this is based on the upper limit of sizes that are undetectable, this approach can lead to conservative estimates for fatigue life [3].

An ideal means to determine fatigue life would be to grow a crack from an actual initial flaw size (IFS) to a maximum permissible crack size with the use of a crack growth model accurate for very short cracks. However, this is difficult since the IFS would be smaller than the minimum detectable flaw size, and so too small to determine. The behaviour of such small cracks is also heavily influenced by the material's microstructure [4], and so the accurate application of a crack growth model would be difficult. Also, the structure's microstructure is likely to contain many small flaws, and so accurately determining which of these is likely to become a crack is difficult. An approach that would avoid the above problems would involve the use of an equivalent initial flaw size (EIFS). The EIFS is not an actual physical quantity, but can be thought of as a model calibration parameter for which a long-crack growth model can be used [5]. The EIFS provides a helpful starting point for determining the fatigue life of the structure, and of other similar structures under similar conditions.

One of the most common techniques that has been used in the past to determine EIFS is back-extrapolation [6-16], which involves extrapolating inspected cracks backwards to some initial time through the use of a crack growth model. However, its application is limited due to the large amount of fatigue crack growth data needed and the required use of fractography techniques to ensure a high degree of accuracy.

An approach that avoids back-extrapolation involves the use of the El-Haddad model [17] with the Kitagawa-Takahashi diagram [15, 18-21]. In this approach, the calculated EIFS is independent of load history, and only depends on the material properties, fatigue limit and threshold stress intensity factor. One limitation of this approach is that it involves the use of the geometry factor Y, which may be difficult to calculate for complex geometries or multiple cracks [5].

Statistical approaches [5, 22-24], involving the use of Bayesian updating [5, 23, 24] or maximum likelihood estimation (MLE) [5, 22], treat the EIFS as a model calibration parameter. In this method, the most likely EIFS Distribution (EIFSD), given inspection data, is determined. One drawback of the procedures used in [5, 22, 23] is that the combined uncertainty from multiple different sources is represented by a single noise term with an arbitrarily assumed distribution (normal or lognormal). A more robust approach would involve taking into account individual sources of uncertainty [24]. By taking into account individual sources of uncertainty, which can be individually quantified, a more accurate estimate for the EIFSD can be obtained.

One example of a previous work concerning the estimation of the EIFS for Multiple Site Damage (MSD) is Kim et al. [12], where the back extrapolation technique coupled with the Extended Finite Element Method (XFEM) was used to obtain the EIFSD for a specimen with multiple simultaneous cracks emanating from fastener holes. Renaud et al. [13] used the back extrapolation method with an optimization based methodology to determine the EIFS for MSD in the CC-130 aircraft. It was found that results matched well with in-service findings. Kim et al. [14] built on their previous work in [12] by interfacing Kriging with XFEM to develop a probabilistic approach to the EIFS for MSD, involving the consideration of multiple sources of uncertainty. Although back extrapolation has found a great deal of use in the calculation of the EIFSD for MSD, the employment of statistical methods such as Bayesian updating has not been considered. Statistical methods are able to provide an EIFSD independent of load history, making the resulting EIFSD more applicable to the fatigue life analysis

of other similar structures. This work aims to employ Bayesian updating for the purpose of obtaining the EIFSD of a structural component in the presence of MSD.

A Dual Boundary Element Method (DBEM) model can be computationally expensive to run if there are many cracks to consider, as is the case in this work. In order to ensure that the proposed methodology for the statistical inference of the EIFSD can be practically applied, multi-fidelity modelling, a form of surrogate modelling that makes use of low-fidelity and high-fidelity model data, is used in this work to create computationally-cheap substitute models that act in place of the expensive DBEM models for the statistical inference of the EIFSD. In this work, low-fidelity and high-fidelity models refer to models which have coarse and fine meshes respectively. Multi-fidelity modelling has found a great deal of use in the field of structural analysis due to the significant improvements in efficiency that it can provide. A past example of multi-fidelity modelling is Morse et al. [25] where multi-fidelity models, in the form of response surfaces, were used in place of a Boundary Element Method (BEM) model for the structural reliability analysis of a thin plate. Results showed the multi-fidelity models matched the high-fidelity BEM model in terms of accuracy but provided much lower computational costs. Lefebvre at al. [26] employed a more sophisticated approach involving the use of Co-Kriging to create multi-fidelity models for the reliability analysis of a cracked cylinder. Results showed that Co-Kriging could obtain similar levels of accuracy to regular Kriging, but at reduced computational cost.

The main objective of this work concerns the development of a new methodology for the statistical inference, via Bayesian updating, of the EIFSD for a structural component using the Dual Boundary Element Method (DBEM). Bayesian updating is an established technique in the field of reliability engineering [27-29]. It enables new information, such as in the form of data from routine inspections, to be used to update the inferred EIFSD, allowing for the continual improvement of the estimated EIFSD over time. The DBEM is used for the first time for a topic involving the EIFS. The main benefit of the DBEM is that little or no remeshing is required. This benefit, in addition to the inherent benefits of the BEM, such as the reduced dimensionality of the problem and its high accuracy, enables crack growth to be modelled in a highly efficient manner. The application of multi-fidelity modelling for reducing the computational cost of the estimation of the EIFSD is also investigated for the first time. Multi-fidelity modelling, via the surrogate modelling technique Co-Kriging, is used in place of the DBEM model for the computationally-expensive Monte Carlo sampling required for the inference of the EIFSD and could prove to be a more efficient alternative to single-fidelity surrogate modelling techniques used in the past, such as Kriging. In summary, the novel contributions of this work are:

- The DBEM is used for the first time to estimate the EIFSD for a structure. A DBEM-based automatic incremental crack growth procedure, that requires little or no remeshing, is employed for the statistical inference of the EIFSD. It offers a very efficient means to simulate fatigue crack growth.
- Multi-fidelity modelling, via Co-Kriging, is employed for the first time for an application involving determining the EIFSD of a structure. It is used in place of the expensive DBEM model for the statistical inference of the EIFSD and has the potential to provide significant improvements in efficiency. Allowing for more complicated crack configurations to be investigated.
- A methodology for the statistical inference of the EIFSD in a structural component in the presence of MSD, and multiple sources of uncertainty, has been developed for the first time. Previous work on this topic has exclusively involved the use of the back-extrapolation method. One drawback of the back-extrapolation approach is that a large amount of data is required. The proposed statistical inference methodology avoids this problem by treating the EIFS as a model calibration parameter, whereby the most likely EIFSD is determined based on simulated inspection data from a fleet of aircraft.

1.1. Incremental Crack Growth Procedure

The dual boundary element method (DBEM) developed in [30] is employed here for modelling crack problems. The discretised equations for the DBEM can be written in a compact form as:

$$\boldsymbol{C}\boldsymbol{u} + \sum_{n=1}^{N_e}\left(\int_{\Gamma_n} \boldsymbol{T}\boldsymbol{\psi}^{\boldsymbol{T}}\boldsymbol{d}\Gamma\right)\boldsymbol{u}^n + \sum_{n=1}^{N_c}\left(\int_{\Gamma_n} \boldsymbol{T}\boldsymbol{\psi}^{\boldsymbol{T}}\boldsymbol{d}\Gamma\right)\Delta\boldsymbol{u}^n = \sum_{n=1}^{N_c}\left(\int_{\Gamma_n} \boldsymbol{U}\boldsymbol{\psi}^{\boldsymbol{T}}\boldsymbol{d}\Gamma\right)\boldsymbol{t}^n \qquad (1)$$

for the displacement boundary integral equation, and:

$$\frac{\mathbf{1}}{\mathbf{2}}\boldsymbol{t} + \sum_{n=1}^{N_e}\boldsymbol{n}\left(\int_{\Gamma_n} \boldsymbol{S}\boldsymbol{\psi}^{\boldsymbol{T}}\boldsymbol{d}\Gamma\right)\boldsymbol{u}^n + \sum_{n=1}^{N_c}\boldsymbol{n}\left(\int_{\Gamma_n} \boldsymbol{S}\boldsymbol{\psi}^{\boldsymbol{T}}\boldsymbol{d}\Gamma\right)\Delta\boldsymbol{u}^n = \sum_{n=1}^{N_c}\boldsymbol{n}\left(\int_{\Gamma_n} \boldsymbol{D}\boldsymbol{\psi}^{\boldsymbol{T}}\boldsymbol{d}\Gamma\right)\boldsymbol{t}^n \qquad (2)$$

for the traction equation. In these equations N_e and N_c are the number of elements on the external and crack surfaces respectively, the boundary of the domain is denoted by Γ, and the free term $\boldsymbol{C}$ denotes 2×2 submatrices. The fundamental solutions (important equations used in the BEM) are denoted as $\boldsymbol{T}, \boldsymbol{U}, \boldsymbol{S}$, and $\boldsymbol{D}$. The vectors $\boldsymbol{u}, \boldsymbol{t},$ and $\Delta\boldsymbol{u}^n$ denote displacements and tractions on the boundary and displacement discontinuity across the crack surfaces, respectively. The vector $\boldsymbol{\psi}$ contains either the isoparametric quadratic shape functions on the boundary or the discontinuous quadratic shape functions on the crack surfaces [31]. When modelling cracks both the upper and lower surfaces of the crack are considered co-planar. Therefore, when the lower and upper surfaces are discretised, the nodes of an element on the lower surface will share the same coordinates as the nodes on the opposing element on the upper surface. This can lead to mathematical degeneration. The DBEM avoids the issues associated with co-planar crack surfaces by applying the displacement integral equation for collocation on the upper crack surface, and the traction integral equation for collocation on the lower surface. This enables crack problems to be solved with a single-region formulation.

The simulation of fatigue crack growth involves an incremental crack extension analysis. In this procedure cracks are automatically grown in an incremental manner from a specified initial crack size to a specified final crack size. The mode I and mode II stress intensity factors for the crack tips are calculated using the mixed-mode J-integral. Because the BEM provides a continuous modelling of the interior of the structure, with no discretisation required, the use of the J-integral is especially effective. The direction of the incremental extensions are determined using the maximum principal stress criterion, while the Paris law in [32] is used to calculate the size of the extension and the number of loading cycles required for the crack to grow this amount. The incremental extension of the crack is modelled by adding new elements (i.e. 2 elements) at the crack tip(s). This automatic incremental crack growth procedure [33] requires little or no remeshing. For conciseness, a short introduction to the procedure is given. More detailed descriptions can be found in [31, 33, 34]. The incremental growth of a crack using this method can be seen in Figure 1.1

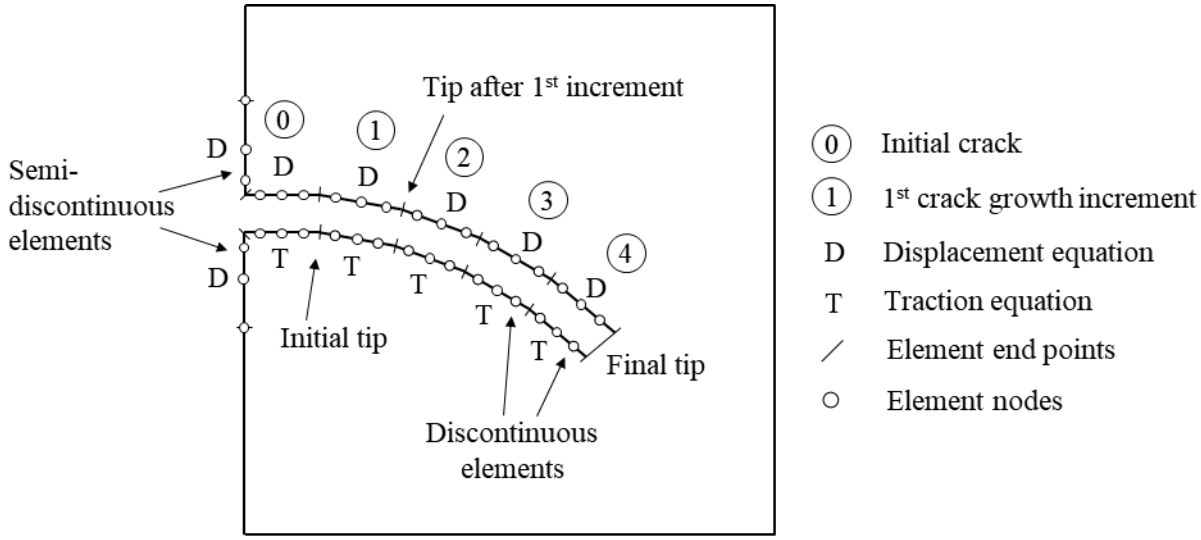

Figure 1.1 here

Figure 1.1. Incremental growth of an edge crack in a square plate. Quadratic elements are used. The upper and lower surfaces of the crack are assumed to be coplanar.

The system of equations used in the BEM is of the form $\boldsymbol{Hu} = \boldsymbol{Gt}$, where $\boldsymbol{H}$ and $\boldsymbol{G}$ are matrices of coefficients, and $\boldsymbol{u}$ and $\boldsymbol{t}$ are vectors containing boundary displacements and tractions respectively. This system of equations can be rearranged in the form $\boldsymbol{AX} = \boldsymbol{F}$, where $\boldsymbol{X}$ is a vector that contains all the unknown boundary displacements and tractions, $\boldsymbol{A}$ is a matrix of known coefficients, and $\boldsymbol{F}$ is a vector containing known coefficients multiplied by known tractions. The vector $\boldsymbol{X}$ can be calculated by LU decomposition. The rows and columns of $\boldsymbol{A}$, $\boldsymbol{X}$, and $\boldsymbol{F}$ correspond to elements used to discretise the boundary of a structure. To model the growth of a crack, new elements are added to the tip of the crack, this results in new rows and columns being added to the already existing system of equations. This process is demonstrated in Figure 1.2. For each increment, only the newly added rows and columns need to be LU-decomposed since the already LU-decomposed rows and columns are carried over from one growth increment to another. This approach therefore offers a very efficient means to model crack growth.

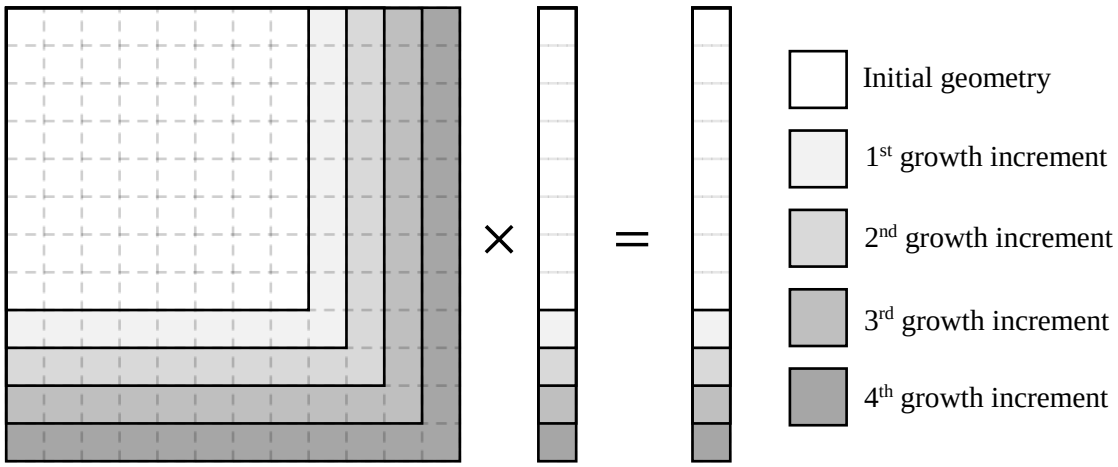

Figure 1.2 here

Figure 1.2. Automatic updating of the system of equations $\boldsymbol{AX} = \boldsymbol{F}$. New rows and columns are added for each crack growth increment.

The number of cycles N required for a crack to grow one increment Δa is given by:

$$N = \int_{a_0}^{a_1} \frac{1}{da/dN}\, da \tag{3}$$

where a_0 and a_1 are the lengths of the crack before and after the current growth increment, and da/dN is the crack growth rate. The size of the crack growth increment ($\Delta a = a_1 - a_0$) can be specified. The integration in Eq. (3) was performed using Simpson's rule with 8 subdivisions, as this number was found to provide sufficiently accurate results during preliminary testing. If a structure contains a total of M ($M > 1$) simultaneous cracks, the critical crack will grow the prescribed amount Δa for each increment while the sub-critical cracks will each grow by different smaller amounts given by $\varphi_i \Delta a$ ($i = 1,2, \dots, M$), where φ_i ($\varphi_i \leq 1$) is the scaling factor for the i'th crack. This scaling factor is determined by comparing the growth rates of the individual cracks with the growth rate of the critical crack. In this approach, the stress intensity factors are determined for each of the M cracks, then the number of cycles required for each crack to grow an incremental amount Δa is determined. The critical crack is identified as the crack which requires the least amount of cycles (N_{min}) to grow by the amount Δa. The crack growth increments $\varphi_i \Delta a$ for the sub-critical cracks are then determined by calculating the amount each crack will grow in N_{min} cycles. This process is repeated for each increment of growth. The direction of growth for each increment is determined using the maximum principal stress criterion. Once the number of cycles corresponding to each increment has been calculated, they are summed up to provide the total number of cycles required to grow the cracks from their specified initial sizes to their specified final sizes.

Using Paris's law, the crack growth rate is:

$$\frac{da}{dN} = C\left(\Delta K_{eff}\right)^m \tag{4}$$

where C and m are the Paris law constants. The effective stress intensity factor range $\Delta K_{eff} = K_{eff}^{max} - K_{eff}^{min}$ (where the superscripts max and min refer to K_{eff} evaluated at the maximum and minimum stress levels respectively) was experimentally derived by Tanaka [35], and takes into account the effects of both mode I and mode II crack deformation:

$$\Delta K_{eff} = \sqrt{\Delta K_I^2 + 2\Delta K_{II}^2} \tag{5}$$

where ΔK_I and ΔK_{II} are the stress intensity factor ranges for mode I and mode II crack deformation respectively and are calculated using the J-integral method [31].

Both C and m are dependent on the material used. C is also dependent on the stress ratio R ($R = \sigma_{min}/\sigma_{max}$). This relationship was modelled using Walker's equation [36]:

$$C = \frac{C_0}{(1-R)^{m(1-\gamma)}} \tag{6}$$

where C_0 is the value of C when $R = 0$, and γ is a material constant.

1.2. Statistical Inference of the EIFSD for MSD

In this work, Bayesian updating is used to infer the EIFSD of a structure in the presence of MSD. Bayesian updating involves using new information, such as data obtained from inspections, to update prior assumptions regarding the probability of an event. Bayes's rule is:

$$P(H|D) = \frac{P(D|H)P(H)}{P(D)} \tag{7}$$

where $P(H|D)$ is the posterior probability of a hypothesis H being true given some data D, $P(D|H)$ is the likelihood of D given H, $P(H)$ is the prior probability of H or the probability that H is true before being given D, and $P(D)$ is a normalising factor that ensures the integral of $P(H|D)$ over the predefined domain is equal to 1. In this work, Bayesian updating is used to infer the statistical

parameters (mean and standard deviation) of the EIFSD in the presence of multiple sources of uncertainty. EIFS is denoted as θ.

Given that lognormal distributions are commonly used to model distributions for parameters such as fatigue life and crack sizes [37], it is assumed for the EIFSD and the likelihood function in this work. Given that a total of M^{ins} inspections were carried out, and given that the i'th inspection ($i = 1,2,\dots,M^{ins}$) occurred at N_i^{ins} cycles, and that the inspection detected a total of M_i^{crk} cracks, the likelihood that some guess $\hat{\theta}$ for the EIFS is the true EIFS for the j'th crack of the i'th inspection $\left(j = 1,2,\dots,M_i^{crk}\right)$ of size a_{ij} is:

$$L\left(\hat{\theta}|N_i^{ins}, a_{ij}, \boldsymbol{Y}\right) = f_{N|\hat{\theta},a_{ij},\boldsymbol{Y}}\left(N_i^{ins}|\hat{\theta}, a_{ij}, \boldsymbol{Y}\right) = \frac{1}{N_i^{ins}\sqrt{2\pi\beta^2}}\exp\left(-\frac{\left[\log\left(N_i^{ins}\right)-\alpha\right]^2}{2\beta^2}\right) \quad (8)$$

The number of cycles required to grow the j'th crack of the i'th inspection from $\hat{\theta}$ to a_{ij} is represented by the distribution $f_{N|\hat{\theta},a_{ij},\boldsymbol{Y}}$. This is because there is uncertainty in the parameters that influence crack growth, namely: C, m, σ_{max}, and R. The uncertainty in these parameters is represented by the vector $\boldsymbol{Y}$. The distribution $f_{N|\hat{\theta},a_{ij},\boldsymbol{Y}}$ was found to closely resemble a lognormal distribution and has a mean α and standard deviation β. This distribution can be estimated using Monte Carlo sampling by considering the uncertainty in C, m, σ_{max}, and R. The number of cycles N_{ij} required to grow the j'th crack of the i'th inspection from $\hat{\theta}$ to a_{ij} in the presence of the other cracks found during the inspection can be estimated using some crack growth model: $F_{ij}\left(C, m, \sigma_{max}, R, \hat{\theta}\right)$. For each Monte Carlo sample, the values of C, m, σ_{max}, and R are chosen randomly per their probability distributions. To accurately estimate a probability distribution using Monte Carlo sampling, thousands of simulations are often required. Once the distribution has been estimated, α and β can be calculated and the likelihood shown in Eq. (8) can be obtained. A diagram showing this procedure can be seen in Figure 1.3.

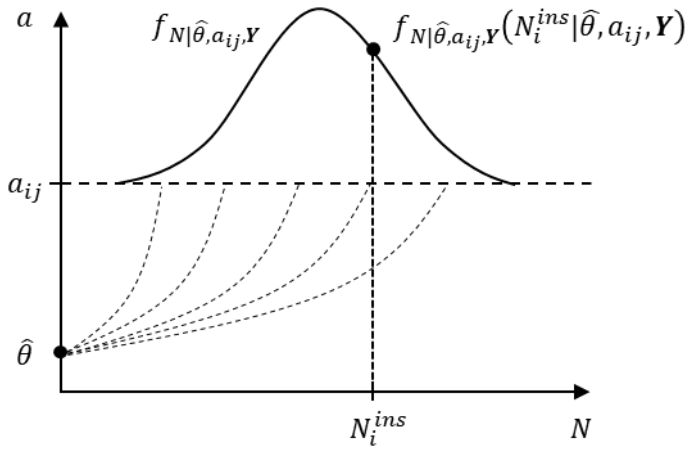

Figure 1.3 here

Figure 1.3. The distribution $f_{N|\hat{\theta},a_{ij},\boldsymbol{Y}}$.

Because of the many runs of the crack growth model F_{ij} required for Monte Carlo sampling, it would be computationally expensive to use a DBEM model as F_{ij}. Therefore, Co-Kriging models are used in this work in place of DBEM models for this sampling. These Co-Kriging models will be created based on DBEM models.

The likelihood that $\hat{\theta}$ is the true EIFS for all of the cracks in the i'th inspection is given by the assumption:

$$L\left(\hat{\theta}|\boldsymbol{D}_i,\boldsymbol{Y}\right)=\prod_{j=1}^{M_i^{crk}}L\left(\hat{\theta}|N_i^{ins},a_{ij},\boldsymbol{Y}\right) \tag{9}$$

where $\boldsymbol{D}_i=\left(N_i^{ins},\boldsymbol{a_i}\right)$ is a vector containing the data from the i'th inspection, where the row vector $\boldsymbol{a}_i=\left(a_{i1},a_{i2},\ldots,a_{iM_i^{crk}}\right)$. The likelihood that some combination of guesses mean $\hat{\mu}$ and standard deviation $\hat{\sigma}$ are the actual values, μ and σ, of the true EIFSD, given the data from the i'th inspection is:

$$L(\hat{\mu},\hat{\sigma}|\boldsymbol{D}_i,\boldsymbol{Y})=\int L\left(\hat{\theta}|D_i,\boldsymbol{Y}\right)f_\theta\left(\hat{\theta}|\hat{\mu},\hat{\sigma}\right)d\hat{\theta} \tag{10}$$

where $f_\theta\left(\hat{\theta}|\hat{\mu},\hat{\sigma}\right)$ is an EIFSD with parameters $\hat{\mu}$ and $\hat{\sigma}$ evaluated at $\hat{\theta}$. The individual likelihood functions are:

$$L(\hat{\mu}|\boldsymbol{D}_i,\boldsymbol{Y})=\int L(\hat{\mu},\hat{\sigma}|\boldsymbol{D}_i,\boldsymbol{Y})d\hat{\sigma} \tag{11}$$

$$L(\hat{\sigma}|\boldsymbol{D}_i,\boldsymbol{Y})=\int L(\hat{\mu},\hat{\sigma}|\boldsymbol{D}_i,\boldsymbol{Y})d\hat{\mu} \tag{12}$$

Posterior estimates for the actual probability distributions of μ and σ are:

$$f_{\mu|\boldsymbol{D}_i,\boldsymbol{Y}}(\hat{\mu}|\boldsymbol{D}_i,\boldsymbol{Y})=\frac{L(\hat{\mu}|\boldsymbol{D}_i,\boldsymbol{Y})f_{\mu|\boldsymbol{D}_{i-1},\boldsymbol{Y}}(\hat{\mu}|\boldsymbol{D}_{i-1},\boldsymbol{Y})}{\int L(\hat{\mu}|\boldsymbol{D}_i,\boldsymbol{Y})f_{\mu|\boldsymbol{D}_{i-1},\boldsymbol{Y}}(\hat{\mu}|\boldsymbol{D}_{i-1},\boldsymbol{Y})d\hat{\mu}} \tag{13}$$

$$f_{\sigma|\boldsymbol{D}_i,\boldsymbol{Y}}(\hat{\sigma}|\boldsymbol{D}_i,\boldsymbol{Y})=\frac{L(\hat{\sigma}|\boldsymbol{D}_i,\boldsymbol{Y})f_{\sigma|\boldsymbol{D}_{i-1},\boldsymbol{Y}}(\hat{\sigma}|\boldsymbol{D}_{i-1},\boldsymbol{Y})}{\int L(\hat{\sigma}|\boldsymbol{D}_i,\boldsymbol{Y})f_{\sigma|\boldsymbol{D}_{i-1},\boldsymbol{Y}}(\hat{\sigma}|\boldsymbol{D}_{i-1},\boldsymbol{Y})d\hat{\sigma}} \tag{14}$$

where $f_{\mu|D_i,\boldsymbol{Y}}(\hat{\mu}|\boldsymbol{D}_i,\boldsymbol{Y})$ denotes a posterior estimate for the distribution of μ given $\boldsymbol{D}_i$ and $\boldsymbol{Y}$, evaluated at $\hat{\mu}$. The integrations seen in equations (10)-(14) were carried out with the Trapezoidal rule. A total of 50 evenly spaced integration points/guesses were used for each of the variables $\hat{\theta}$, $\hat{\mu}$, and $\hat{\sigma}$.

Once the data from a new inspection is available, the process repeats through equations (8) to (14), and the posterior distributions $f_{\mu|\boldsymbol{D}_i,\boldsymbol{Y}}$ and $f_{\sigma|\boldsymbol{D}_i,\boldsymbol{Y}}$ are updated using Baye's rule (equations (13) and (14)). The posterior distributions from the previous inspection are used as the prior distributions, $f_{\mu|\boldsymbol{D}_{i-1},\boldsymbol{Y}}$ and $f_{\sigma|\boldsymbol{D}_{i-1},\boldsymbol{Y}}$, for the new inspection. Once $f_{\mu|\boldsymbol{D}_i,\boldsymbol{Y}}$ and $f_{\sigma|\boldsymbol{D}_i,\boldsymbol{Y}}$ have been obtained after the i'th inspection, the mean of these distributions $\mu_{\theta,i}=E(\mu)$ and $\sigma_{\theta,i}=E(\sigma)$ are calculated. This is demonstrated in Figure 1.4.

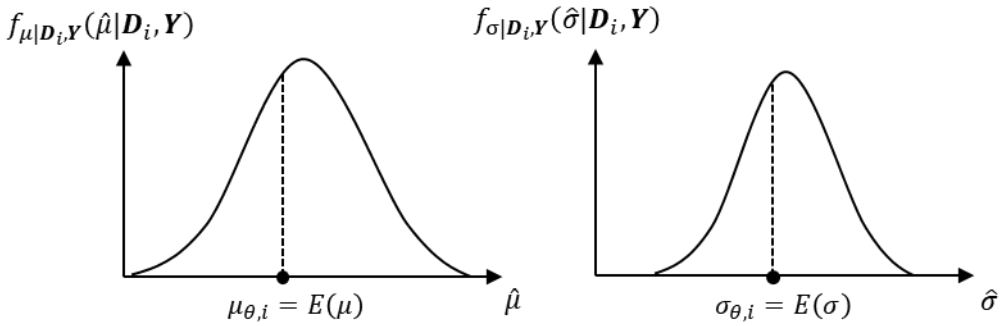

Figure 1.4 here

Figure 1.4. The posterior distributions $f_{\mu|\boldsymbol{D}_i,\boldsymbol{Y}}$ and $f_{\sigma|\boldsymbol{D}_i,\boldsymbol{Y}}$ and their mean values $\mu_{\theta,i}$ and $\sigma_{\theta,i}$.

After $\mu_{\theta,i}$ and $\sigma_{\theta,i}$ have been obtained for the i'th inspection, the average of these values and the previous values is calculated:

$$\bar{\mu}_{\theta,i} = \frac{1}{i}\sum_{k=1}^{i}\mu_{\theta,k} \qquad \bar{\sigma}_{\theta,i} = \frac{1}{i}\sum_{k=1}^{i}\sigma_{\theta,k} \tag{15}$$

These two values are then used as the mean and standard deviation of our estimate for the EIFSD after the i'th inspection. This is demonstrated in Figure 1.5. As mentioned earlier the EIFSD is assumed to follow a lognormal distribution.

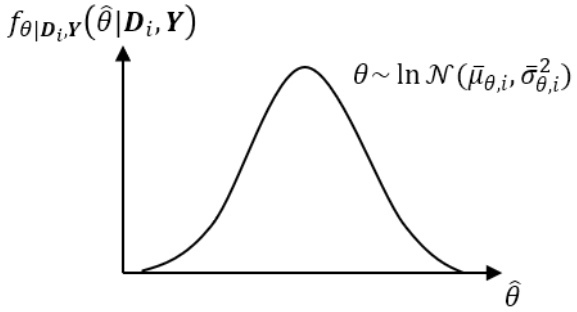

Figure 1.5 here

Figure 1.5. Estimate for the EIFSD after the i'th inspection.

A flowchart showing the steps of the proposed methodology is shown in Figure 1.6. The procedure for Bayesian updating can be stopped after a certain number of inspections have been carried out. This number can be determined by the engineer. Generally, more inspections lead to a more accurate estimate for the EIFSD. The initial prior distributions, $f_{\mu|\boldsymbol{D}_0,\boldsymbol{Y}}$ and $f_{\sigma|\boldsymbol{D}_0,\boldsymbol{Y}}$, can be chosen based on hypothetical prior experience or knowledge regarding the EIFSD on behalf of the engineer. If no prior experience or knowledge is available, then uniform distributions can be chosen for these initial prior distributions.

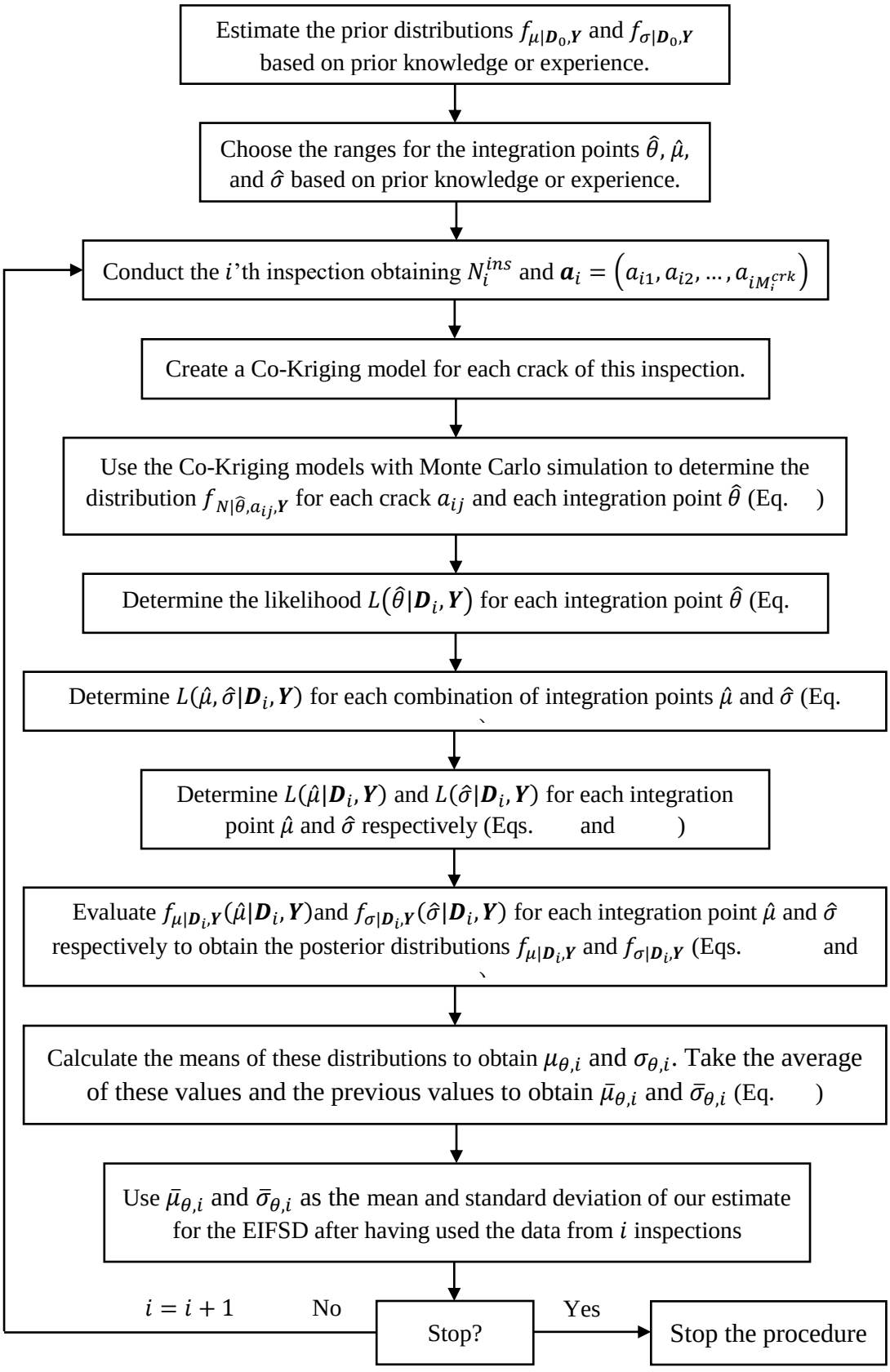

Figure 1.6. Flowchart of the proposed methodology for the statistical inference of the EIFSD.

Figure 1.6 here

1.3. Multi-Fidelity Modelling with Co-Kriging

Co-Kriging is an advanced form of Kriging; an interpolation method that involves modelling interpolated values as a Gaussian process. Kriging has proven to be very effective for the creation of surrogate models; cheap models that are used in place of expensive models but can achieve similar levels of accuracy. Since Kriging interpolates the data points used in the creation of the surrogate model, it is ideally suited for use with computer programs since they are deterministic in nature. Co-Kriging takes into account not only expensive/high-fidelity model data when creating the surrogate model, but also cheap/low-fidelity model data. By also taking into account low-fidelity data, it is expected that a smaller amount of high-fidelity data is required to achieve the same accuracy as a Kriging model using a larger amount of high-fidelity data, leading to less CPU-time required to create the Co-Kriging model overall compared to the Kriging model.

To create a surrogate model, deign data is required. This is typically composed of a matrix of design sites and a column vector of outputs. The matrix of design sites $\boldsymbol{S}$ contains n combinations of the m input variables. The vector of outputs $\boldsymbol{Y}$ of length n contains the responses of a computer model to the n combination in $\boldsymbol{S}$. $\boldsymbol{S}$ and $\boldsymbol{Y}$ are:

$$\boldsymbol{S} = \begin{bmatrix} \boldsymbol{s}_1 \\ \boldsymbol{s}_2 \\ \vdots \\ \boldsymbol{s}_n \end{bmatrix} = \begin{bmatrix} s_{11} & s_{12} & \cdots & s_{1m} \\ s_{21} & s_{22} & \cdots & s_{2m} \\ \vdots & \vdots & \ddots & \vdots \\ s_{n1} & s_{n2} & \cdots & s_{nm} \end{bmatrix} \tag{16}$$

$$\boldsymbol{Y} = \begin{bmatrix} y(\boldsymbol{s}_1) \\ y(\boldsymbol{s}_2) \\ \vdots \\ y(\boldsymbol{s}_n) \end{bmatrix} = \begin{bmatrix} Y_1 \\ Y_2 \\ \vdots \\ Y_n \end{bmatrix} \tag{17}$$

The methodology involved in determining the combinations of design sites in $\boldsymbol{S}$ is known as the Design and Analysis of Computer Experiments (DACE). There are three main types of designs that are used with DACE, these are random sampling, stratified sampling, and quasi-random sequences [38]. In the third type, quasi-random sequences, the design sites are chosen in consideration of previous design sites, ensuring that they are evenly spread, thereby preventing the occurrence of clusters and gaps. Therefore, surrogate models created using this technique could prove to be more accurate than those created with other techniques such as Latin Hypercube sampling [39], while also requiring less design sites in their creation. Therefore, in this work, a type of quasi-random sequence known as Sobol sequences [38] are used to generate the design sites in $\boldsymbol{S}$.

Due to the use of random variables in this work, a form of importance sampling is used to ensure that the design sites are more concentrated in the most likely regions of each variable's domain. By default, the design points obtained from a Sobol sequence lie in the range (0,1). The inverse Cumulative Distribution Function (CDF) of these design points are taken for each variable to obtain new design points. The new design points are therefore more concentrated in the most-likely regions of each variable's domain, and less concentrated in the least-likely regions.

1.3.1.*Kriging*

For conciseness, a brief introduction to Kriging is provided. A comprehensive introduction to Kriging can be found in [40].

A Kriging model is of the form:

$$\hat{y}(\boldsymbol{x}) = \boldsymbol{f}^{\mathrm{T}}(\boldsymbol{x})\boldsymbol{\beta} + Z(\boldsymbol{x}) \tag{18}$$

where $\hat{y}(\boldsymbol{x})$ is termed the Kriging predictor and is the output of the Kriging model at some trial point $\boldsymbol{x}$ ($\boldsymbol{x} = [x_1, x_2, \ldots, x_m]$), $\mathbf{f}$ and $\boldsymbol{\beta}$ are column vectors of length p containing regression functions and regression coefficients respectively, and Z is a stationary Gaussian process that models the interpolated values. The covariance of Z is:

$$\mathrm{cov}[Z(\boldsymbol{s}_i), Z(\boldsymbol{x})] = \mathrm{E}[Z(\boldsymbol{s}_i)Z(\boldsymbol{x})] = \sigma^2 \mathcal{R}(\boldsymbol{\theta}, \boldsymbol{s}_i, \boldsymbol{x}) \tag{19}$$

where E denotes expectation, and σ^2 is the process variance. The correlation function $\mathcal{R}$ represents the correlation between the design points $\boldsymbol{s}_i$, $s_{ij} \in \mathbb{R}^{n \times m}$, and the trial point $\boldsymbol{x}$. The hyperparameters $\boldsymbol{\theta}$, $\theta_j \in \mathbb{R}^m$, describe the level of influence that the distance between the design points $\boldsymbol{s}_i$ and $\boldsymbol{x}$ have on $\mathcal{R}$. The most commonly used correlation function $\mathcal{R}$ is the Gaussian correlation function due to its ability to provide an approximation surface that is smooth and infinitely differentiable [40]. It is used in this work and is given by:

$$\mathcal{R}(\boldsymbol{\theta}, \boldsymbol{s}_i, \boldsymbol{x}) = \prod_{j=1}^{m} \mathcal{R}(\theta_j, s_{ij}, x_j) = \prod_{j=1}^{m} \exp\left(-\theta_j \left| s_{ij} - x_j \right|^2\right) = \exp\left(\sum_{j=1}^{n} \left(-\theta_j d_j^2\right)\right) \tag{20}$$

where $d_j = \left| s_{ij} - x_j \right|$.

1.3.2. *Co-Kriging*

A Co-Kriging model exploits the correlation between the response of a cheap/low-fidelity model and an expensive/high-fidelity model. Two sets of design data are used in Co-Kriging, the set of the cheap/low-fidelity data $(\boldsymbol{S}_c, \boldsymbol{Y}_c)$ where $\boldsymbol{S}_c$ is a $n_c \times m$ matrix and $\boldsymbol{Y}_c$ is a column vector of length n_c, and an expensive/high-fidelity set $(\boldsymbol{S}_e, \boldsymbol{Y}_e)$ where $\boldsymbol{S}_e$ is a $n_e \times m$ matrix and $\boldsymbol{Y}_e$ is a column vector of length n_e. A brief introduction to the formulations for Co-Kriging is provided here. A more detailed description of the formulations can be found in [41].

Co-Kriging can be thought of as involving the creation of two Kriging models in sequence, one that approximates the output of the cheap/low-fidelity model $\boldsymbol{Y}_c$, and one that approximates the residuals $\boldsymbol{Y}_d$ between the expensive/high-fidelity output $\boldsymbol{Y}_e$ and the output of the cheap Kriging model $\hat{y}_c$. This can be presented as:

$$\boldsymbol{Y}_d = \boldsymbol{Y}_e - \rho \hat{y}_c(\boldsymbol{S}_e) \tag{21}$$

where ρ is a scaling parameter estimated using Maximum Likelihood Estimation (MLE). The relationship between the Gaussian processes evaluated at some trial point $\boldsymbol{x}$ is:

$$Z_e(\boldsymbol{x}) = Z_d(\boldsymbol{x}) + \rho Z_c(\boldsymbol{x}) \tag{22}$$

Similar to the covariance seen in Eq. (19), the elements of the covariance matrix in this case are:

$$\mathrm{cov}[Z_c(\boldsymbol{S}_c), Z_c(\boldsymbol{S}_c)] = \sigma_c^2 \mathcal{R}(\boldsymbol{\theta}_c, \boldsymbol{S}_c, \boldsymbol{S}_c) \tag{23}$$

$$\mathrm{cov}[Z_c(\boldsymbol{S}_c), Z_e(\boldsymbol{S}_e)] = \rho \sigma_c^2 \mathcal{R}(\boldsymbol{\theta}_c, \boldsymbol{S}_c, \boldsymbol{S}_e) \tag{24}$$

$$\mathrm{cov}[Z_e(\boldsymbol{S}_e), Z_e(\boldsymbol{S}_e)] = \rho^2 \sigma_c^2 \mathcal{R}(\boldsymbol{\theta}_c, \boldsymbol{S}_e, \boldsymbol{S}_e) + \sigma_d^2 \mathcal{R}(\boldsymbol{\theta}_d, \boldsymbol{S}_e, \boldsymbol{S}_e) \tag{25}$$

The covariance matrix (dimensions: $(n_c + n_e) \times (n_c + n_e)$) is:

$$\boldsymbol{C} = \begin{bmatrix} \sigma_c^2 \mathcal{R}(\boldsymbol{\theta}_c, \boldsymbol{S}_c, \boldsymbol{S}_c) & \rho \sigma_c^2 \mathcal{R}(\boldsymbol{\theta}_c, \boldsymbol{S}_c, \boldsymbol{S}_e) \\ \rho \sigma_c^2 \mathcal{R}(\boldsymbol{\theta}_c, \boldsymbol{S}_e, \boldsymbol{S}_c) & \rho^2 \sigma_c^2 \mathcal{R}(\boldsymbol{\theta}_c, \boldsymbol{S}_e, \boldsymbol{S}_e) + \sigma_d^2 \mathcal{R}(\boldsymbol{\theta}_d, \boldsymbol{S}_e, \boldsymbol{S}_e) \end{bmatrix} \tag{26}$$

where σ_c^2 and σ_d^2 are the process variances, and $\boldsymbol{\theta}_c$ and $\boldsymbol{\theta}_d$ are the hyperparameters corresponding to the Kriging models for the cheap and residual data respectively. The optimal values of these parameters, and ρ, can be found using MLE [41].

The Co-Kriging approximation of the expensive model is:

$$\hat{y}_e(\boldsymbol{x}) = \boldsymbol{f}^{\mathrm{T}}(\boldsymbol{x})\widehat{\boldsymbol{\beta}} + \boldsymbol{c}^{\mathrm{T}}\boldsymbol{\gamma}^* \tag{27}$$

where $\boldsymbol{\gamma}^* = \boldsymbol{C}^{-1}\left(\boldsymbol{Y} - \boldsymbol{F}\widehat{\boldsymbol{\beta}}\right)$, and $\widehat{\boldsymbol{\beta}} = \left(\boldsymbol{F}^{\mathrm{T}}\boldsymbol{C}^{-1}\boldsymbol{F}\right)^{-1}\boldsymbol{F}^{\mathrm{T}}\boldsymbol{C}^{-1}\boldsymbol{Y}$ are the estimated regression coefficients from MLE, and $\boldsymbol{Y}$ and $\boldsymbol{F}$ are:

$$\boldsymbol{Y} = \begin{bmatrix} \boldsymbol{Y}_c \\ \boldsymbol{Y}_e \end{bmatrix} \tag{28}$$

$$\boldsymbol{F} = \begin{bmatrix} \boldsymbol{F}_c \\ \boldsymbol{F}_e \end{bmatrix} \tag{29}$$

where $\boldsymbol{F}_c$ and $\boldsymbol{F}_e$ are matrices of dimensions $(n_c \times p)$ and $(n_e \times p)$ respectively that contain the design sites $\boldsymbol{S}_c$ and $\boldsymbol{S}_e$ evaluated with the regression functions in $\boldsymbol{f}$. The column vector $\boldsymbol{c}$ of length $(n_c + n_e)$ is:

$$\boldsymbol{c} = \begin{bmatrix} \hat{\rho}\hat{\sigma}_c^2 \mathcal{R}\left(\widehat{\boldsymbol{\theta}}_c, \boldsymbol{S}_c, \boldsymbol{x}\right) \\ \hat{\rho}^2\hat{\sigma}_c^2 \mathcal{R}\left(\widehat{\boldsymbol{\theta}}_c, \boldsymbol{S}_e, \boldsymbol{x}\right) + \hat{\sigma}_d^2 \mathcal{R}\left(\widehat{\boldsymbol{\theta}}_d, \boldsymbol{S}_e, \boldsymbol{x}\right) \end{bmatrix} \tag{30}$$

where the symbol ^ denotes estimates obtained from MLE. In this work, Co-Kriging models are used to replace the expensive DBEM model in the Monte Carlo simulation required to estimate the distribution $f_{N|\widehat{\theta},a_{ij},\boldsymbol{Y}}$ in Eq. (8). The Kriging and Co-Kriging models used in this work are created using the Matlab Kriging toolbox ooDACE [42].

2. Numerical Example – Fuselage Lap Joint Splice

The above methodology was applied to estimate the EIFSD for a fuselage lap joint splice in the presence of Multiple Site Damage (MSD) subjected to constant-amplitude cyclic loading. The splice is composed of Aluminium 2024-T3, with Young's modulus $E = 68.9$ Gpa and Poisson's ratio $\nu = 0.33$. The lap joint has two rows of fastener holes of diameter 5 mm, and pitch 50 mm. The splice is 420 mm in length and 100 mm in width. Quadratic elements were used to model the splice in the BEM. Four elements were used on each of the four outer sides, 12 elements were used for each of the holes on the upper row, and 4 elements were used for each of the holes on the lower row. It is assumed that cracks are more likely to appear on the first row, as seen in the Aloha airlines accident [43]. The holes on this critical row are therefore given more elements to improve accuracy. The BEM model used can be seen in Figure 2.1.

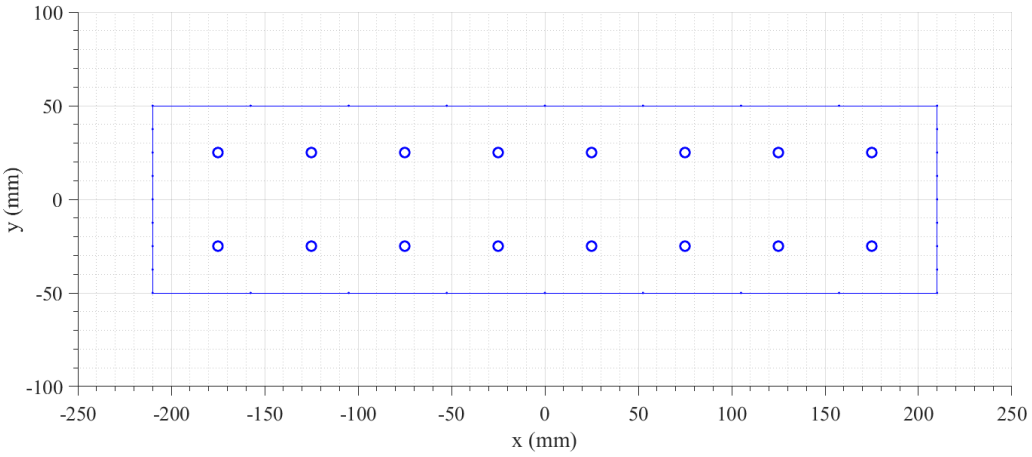

Figure 2.1. The BEM model of the lap joint.

Figure 2.1 here

Cracks in the structure are assumed to be radial cracks emanating from either side of each hole. This gives a possibility of having, at most, 16 cracks in the structure. Therefore, the EIFSD obtained will be the EIFSD for a single type of crack i.e. radial cracks emanating from fastener holes.

The statistical inference was undertaken in the presence of uncertainties in the fatigue model parameters C_0 and m, and in the loading condition parameters σ_{max} and R. These four variables can be modelled as random variables, their statistics can be seen in Table 1. The statistics of C, one of the Paris law constants, can be calculated using the statistics in Table 1 with the Walker equation (Eq. (6)).

Table 1. Random variables and their statistics.

Variable	Distribution	Mean	Coefficient of variation (CoV)
C_0	Lognormal	$1.42 \times 10^{-8}\ \frac{\text{mm/cycle}}{(\text{MPa}\sqrt{\text{m}})^m}$	0.05
m	Lognormal	3.59	0.02
σ_{max}	Lognormal	100 MPa	0.05
R	Lognormal	0.20	0.05

Table 1 here

2.1. Simulation of Inspection Data

For Bayesian updating, new information is required in order to update prior estimates regarding the parameters of the EIFSD. In the current work, this information is in the form of routine inspection simulations carried out on the fuselage lap joint model from a virtual fleet of aircraft. It is assumed that the aircraft are of the same model, subjected to similar loading conditions, and that this particular lap joint is manufactured in the same way for each aircraft. This inspection data includes the number of cycles at which each inspection was carried out, the location of each crack, and the size of each crack. A total of 200 inspections were simulated ($M^{ins} = 200$).

To create the inspection data, an actual EIFSD was chosen. This was chosen to be a lognormal distribution with mean 0.5 mm and standard deviation 0.05 mm. These values were chosen based on EIFS values found in the literature, in which EIFS is typically of the order of several tenths of a millimetre [11, 18, 24]. The size of the critical crack for each inspection a_c (the crack which grows at the fastest rate, and therefore the largest crack present in an inspection and the most likely to be detected) was chosen from a lognormal distribution with mean 5 mm and standard deviation 0.5 mm. This ensures that the difference in crack sizes observed between different inspections is not too great.

It is intuitive that a smaller initial crack leads to a smaller final crack, and vice-versa. Therefore, the actual EIFS for the critical crack, θ_c, and a_c were assumed to be correlated, with an arbitrary correlation coefficient of 0.9. The combination of θ_c and a_c for each inspection was chosen randomly from their corresponding distributions while considering this correlation. The chosen combinations can be seen in Figure 2.2 for the first 100 inspections. The actual EIFS values for the rest of the cracks in each inspection were chosen randomly from the actual EIFSD described earlier.

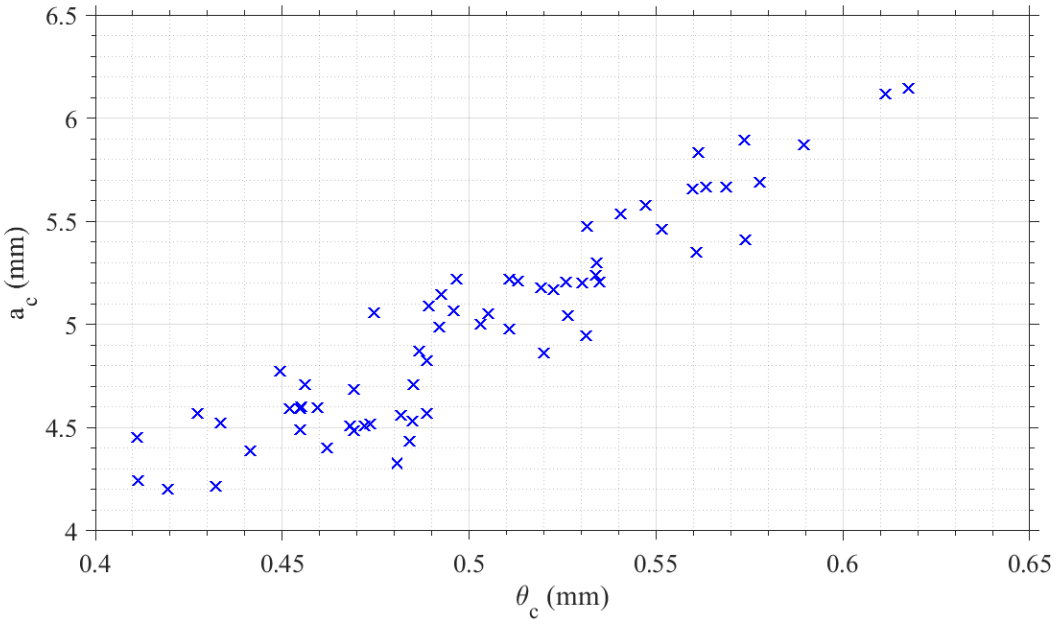

Figure 2.2. Correlation between the actual EIFS θ_c of the critical crack and the inspected size a_c of the critical crack for the first 100 inspections. Each data point represents an inspection.

Figure 2.2 here

The number of cycles required to grow the critical crack from θ_c to a_c, in the presence of all of the other cracks in the inspection, was calculated using the DBEM model with the methodology described in section 1.1. The uncertainties shown in Table 1 were considered in this calculation. This data can be seen in Figure 2.3 for the first 100 inspections.

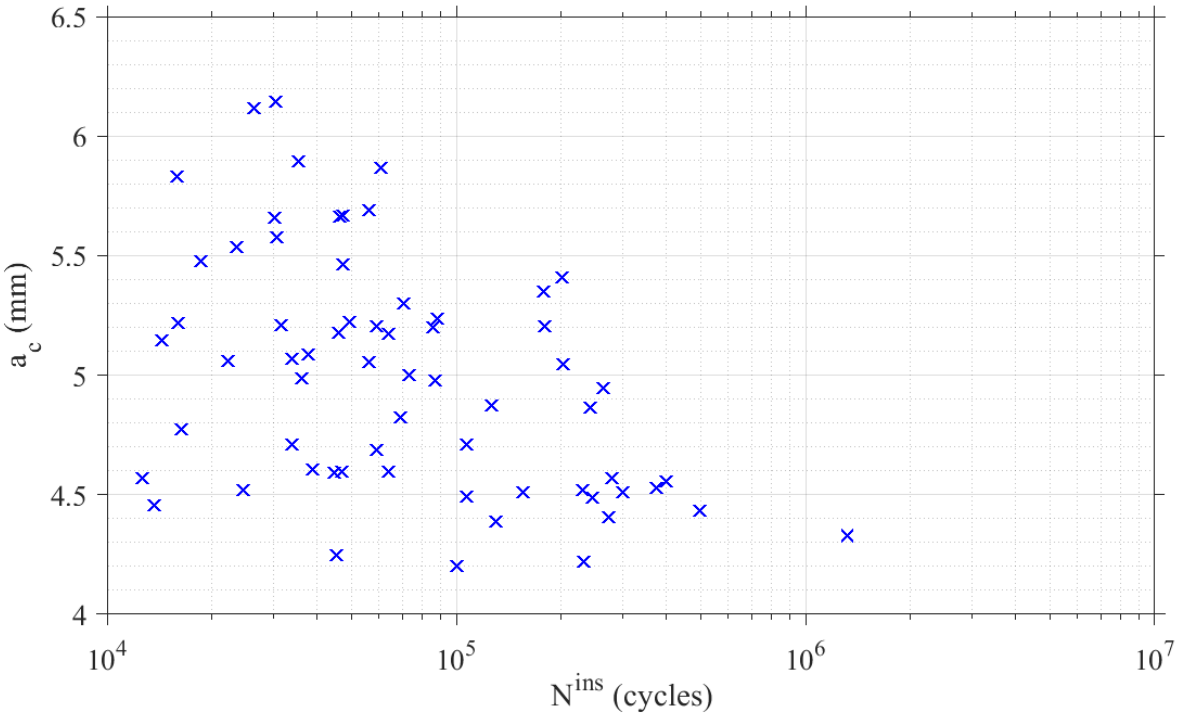

Figure 2.3. Critical crack sizes and number of cycles for each inspection for the first 100 inspections.

Figure 2.3 here

It can be seen in Figure 2.3 that there is a significant amount of variation in the number of cycles for similar critical crack sizes a_{ins}. This suggests that the number of cracks, as well as their locations, significantly influences the rate of crack growth in the lap joint.

An example of the crack distribution in the structure obtained from an inspection can be seen in Figure 2.4.

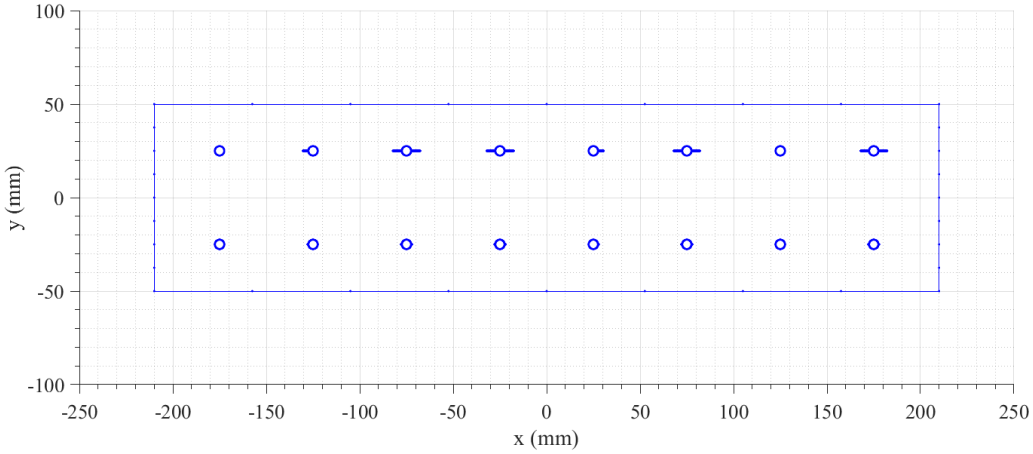

Figure 2.4. A DBEM model showing an example of the crack distribution in the structure obtained from an inspection. There are a total of 10 cracks in this inspection.

Figure 2.4 here

2.2. Multi-Fidelity Modelling

2.2.1. *Monte Carlo sampling*

Co-Kriging models are used to replace the expensive DBEM models for the Monte Carlo sampling required to estimate the distribution $f_{N|\hat{\theta},a_{ij},\boldsymbol{Y}}$ in Eq. (8). This Monte Carlo sampling takes into account uncertainties in the fatigue model parameters C_0 and m, and in the loading condition parameters σ_{max} and R.

The model F_{ij} discussed in section 1.2, as well as being a function of an initial crack size and a final size, is also a function of the four variables in Table 1. A Co-Kriging model F_{ij} can be created for each of the cracks in the i'th inspection, $i = 1,2,\dots,M^{ins}$ (where M^{ins} is the total number of inspections carried out). For the j'th crack, $j = 1,2,\dots,M_i^{crk}$ (where M_i^{crk} is the total number of cracks in inspection i), of inspection i, a Co-Kriging model F_{ij} can be created which calculates the number of cycles N_{ij} required to grow crack ij from $\hat{\theta}$ to its measured size from the inspection, a_{ij}, for different values of C, m, σ_{max}, and R:

$$F_{ij}\left(C, m, \sigma_{max}, R, \hat{\theta}\right) = N_{ij} \tag{31}$$

For a fixed value of $\hat{\theta}$, Monte Caro sampling is carried out using equation (31) with the uncertainties in Table 1 (represented by the vector $\boldsymbol{Y}$). In this approach, the distribution $f_{N|\hat{\theta},a_{ij},\boldsymbol{Y}}$ can be obtained for a particular value of $\hat{\theta}$.

To accurately determine the distribution $f_{N|\hat{\theta},a_{ij},\boldsymbol{Y}}$, many thousands of Monte Carlo samples are required. Given that it would be computationally expensive to carry out this many samples using DBEM models, surrogate models in the form of Co-Kriging models are used instead. These Co-Kriging models are created based on a small number of runs of a low-fidelity and high-fidelity DBEM models.

In both the low-fidelity and high-fidelity DBEM models, the number of elements present prior to crack growth is identical, however, the low-fidelity model uses half the number of elements when growing the cracks from an initial size to a final size. This results in the low-fidelity model only requiring about 30% of the time required by the high-fidelity model to evaluate Eq. (31), but at the cost of reduced accuracy. The increased number of elements used to model the growth of the cracks in the high-fidelity models results in more accurate estimates for the stress intensity factors at the crack tips, and therefore improves the accuracy of the number of cycles required for growth N_{ij}. To reduce the number of calls to the Co-Kriging models, Sobol sampling was used. A total of 10,000 Sobol samples were used to determine each distribution $f_{N|\widehat{\theta},a_{ij},\boldsymbol{Y}}$ as this number was found to provide accurate results during preliminary testing.

2.2.2. *Kriging vs. Co-Kriging*

A total of 200 simulated inspections were carried out for the lap joint seen in Figure 2.1. In order to compare the performance of Kriging with Co-Kriging, both a Kriging model and a Co-Kriging model were created for each inspected crack. The average number of cracks per inspection was 8.14 with a standard deviation of 1.90. Over the 200 inspections there were a total of 1628 cracks, therefore, 1628 Kriging and Co-Kriging models were created. Optimal performance was achieved with Kriging models that were created using 120 high-fidelity design points, while the optimal Co-Kriging models were created using 120 high-fidelity design points and 40 low-fidelity design points. If a lower number of design points were used it was found that the models had poor performance over the required domain, while if a higher number of design points were used the models suffered from poor performance due to over-fitting. On average, the CPU time required to create a Kriging model was about 19.6 CPU minutes, while for a Co-Kriging model is was about 23.0 CPU minutes. This increase of 17.6% can be attributed to the need to calculate the extra 40 low-fidelity design points.

The type regression function and correlation function were chosen to be the same for Kriging and Co-Kriging. The regression function was chosen to be composed of unknown constants (also known as *ordinary* Kriging). The correlation function was of the Matérn class of correlation functions [44]. It was found that these choices for the regression and correlation functions provided the most accurate models.

The time required to run a Co-Kriging model is significantly less than the time required to run a DBEM model. A Co-Kriging model requires on average 0.58 CPU seconds to obtain the 10,000 Sobol samples required by Monte Carlo sampling to estimate the distribution $f_{N|\widehat{\theta},a_{ij},\boldsymbol{Y}}$, while around 249.4 CPU hours are required on average for a DBEM model. The total time required to obtain the final posterior EIFSD using the data from 200 inspections with DBEM models is estimated to be around 3.92×10^7 CPU hours. In comparison, the time associated with the Co-Kriging models, including their creation and use, was around 637.2 CPU hours. This represents a reduction in overall computational cost by a factor of over 61,000.

To test the accuracy of the Kriging and Co-Kriging models, a test dataset was created for each model that was comprised of 1,000 high-fidelity test points that were not used during the design of the model. The creation of each test dataset required 2.84 CPU hours on average. The average error statistics of the 1628 Kriging and Co-Kriging models when run with their test datasets are shown in Table 2. In order to ensure a fair comparison between the Kriging and Co-Kriging models, the 120 high-fidelity design points used to create each Kriging model were also used as the high-fidelity design points for the corresponding Co-Kriging model. Also, for each crack, both types of models had the same test dataset. Therefore, the only difference is the additional 40 low-fidelity design points for each model.

Table 2. Average error statistics for the 1628 Kriging and Co-Kriging models when run with their test datasets.

Error statistic	Kriging	Co-Kriging
Mean Absolute Percentage Error (MAPE) (%)	4.09	3.85
Mean Absolute Error (MAE) (cycles)	3.34×10^3	1.79×10^3
Root Mean Squared Error (RMSE) (cycles)	1.05×10^4	5.79×10^3
Coefficient of determination R^2	0.987	0.997

Table 2 here

The results in Table 2 show that the Co-Kriging models are, on average, more accurate than the Kriging models. Each error statistic is lower for Co-Kriging than Kriging. The error statistic Root Mean Squared Error (RMSE) gives a higher weight to large errors, while Mean Absolute Error (MAE) and Mean Absolute Percentage Error (MAPE) both give the same weight large errors and small errors. Therefore, a high RMSE indicates the presence of relatively large errors/outliers, suggesting poor reliability on behalf of the surrogate model. Given that RMSE for Co-Kriging is 45% lower than for Kriging, this indicates that Co-Kriging provides more reliable results. This is also supported by the fact that Coefficient of determination is higher for Co-Kriging. The lower values of MAPE and MAE for Co-Kriging further demonstrate its good performance.

As stated previously, for each crack the corresponding Kriging and Co-Kriging models were created using the same 120 high-fidelity design points, however, an additional 40 low-fidelity design points were used in the creation of the Co-Kriging models. It was found during the creation of these models and subsequent testing these numbers of design points provided Kriging and Co-Kriging models of optimal performance; minimizing the error statistics seen in Table 2. Using numbers of design points significantly lower or higher than these numbers worsened the performance of the models. It was found during preliminary testing that for the Co-Kriging models to obtain similar levels of error to Kriging with 120 high-fidelity design points, that 80 to 100 high-fidelity design points and an additional 20 to 40 low-fidelity design points needed to be used. This suggests that Co-Kriging is more efficient than Kriging if the same level of error is desired.

The greater reliability of the Co-Kriging models over the Kriging models, even though they both use the same 120 high-fidelity design points, can be explained by the fact that Co-Kriging involves the use of two Kriging models in sequence. One that approximates the low-fidelity model, and a second that approximates the residuals between the high-fidelity model and the output of the low-fidelity Kriging model. The benefit of this is that the Co-Kriging models provide smoother outputs with less outliers. This can be seen in the error statistics shown in Table 2.

The Co-Kriging models require on average 17.6% more time to create than the Kriging models due to the additional 40 low-fidelity design points. However, it has been shown that the addition of these low-fidelity points can provide a significant improvement in accuracy and reliability, making their addition worthwhile. Overall, the Co-Kriging models provided levels of error less than those provided by the Kriging models and at the same time demonstrated a similar level of computational cost. Therefore, they are more effective substitutes for the DBEM model.

2.3. Results and Discussion

As seen in the flowchart shown in Figure 1.6, Bayesian updating requires an initial guess for the prior distributions $f_{\mu|\boldsymbol{D}_0,\boldsymbol{Y}}$ and $f_{\sigma|\boldsymbol{D}_0,\boldsymbol{Y}}$. These prior distributions can be chosen based on the knowledge or experience of the engineer. In this work, three different types of distributions are investigated for $f_{\mu|\boldsymbol{D}_0,\boldsymbol{Y}}$ and $f_{\sigma|\boldsymbol{D}_0,\boldsymbol{Y}}$:

1) Lognormal distributions with statistics far off from the actual statistics (representing poor knowledge on behalf of the engineer).
2) Lognormal distributions with statistics close to the actual statistics (representing good knowledge on behalf of the engineer).
3) Uniform distributions (representing an absence of knowledge on behalf of the engineer).

Bayesian updating is used with each of these three types of initial distributions. The posterior estimates of the EIFSD from Bayesian updating after 25, 50, 100, and 200 inspections have been obtained and are shown in Figures 2.5-2.7. Animations showing the posterior distributions after each inspection can be seen in Figures 2.8-2.10. The values for the mean and standard deviation of the posterior distributions are shown in Tables 3 and 4 respectively.

It can be seen from these figures and tables that for each type of initial distribution the posterior distributions converge towards the actual distribution as the number of inspections carried out increases. It can be said that convergence has been achieved after 100 inspections for each type of initial distribution because the posterior distributions after 100 inspections and after 200 inspections are similar for each of the 3 initial distributions. When an initial distribution of type 2 is used, the posterior distributions converge more quickly, and the converged distribution is closer to the actual distribution. When initial distributions of types 1 & 3 are used the opposite is seen and convergence occurs more slowly, and the converged distributions, although they are very close to the actual distribution, are not as close compared to when an initial distribution of type 2 is used. How close the converged distribution is to the actual distribution is largely dependent on the quality of the initial distribution chosen. It seems that the most effective type of initial distribution is that which is closest to the actual distribution. Uniform distributions seem to be more effective than a poor guess. This suggests that unless the engineer has good knowledge regarding the EIFSD, a uniform distribution should be used. This is intuitive and makes sense. However, even with a poor guess for the initial distribution an accurate estimate for the actual EIFSD can be obtained. This demonstrates the robustness of the proposed methodology for the inference of the EIFSD.

It should be noted that this inspection data would most likely be obtained from a fleet of aircraft of the same model and which experience similar flight conditions. Also, when it is considered that aircraft typically undergo several inspections during their lifetimes, and that there will be many lap-joints present in the aircraft, the collection of data from the inspection of 100 lap joints would not be an overly difficult task. If it is not possible to obtain data from 100 inspections, the data from just 50 inspections would be sufficient to provide posterior distributions with statistics close (within 10 % error) to those of the actual distribution as long as a poor guess is not made for the initial distributions.

In conclusion, the good performance of Bayesian updating with each type of initial distribution suggests that the proposed methodology is accurate and robust when used for the inference of the EIFSD. The proposed methodology was able to approximate the actual distribution within 10% error after the data from 50-100 inspections had been used.

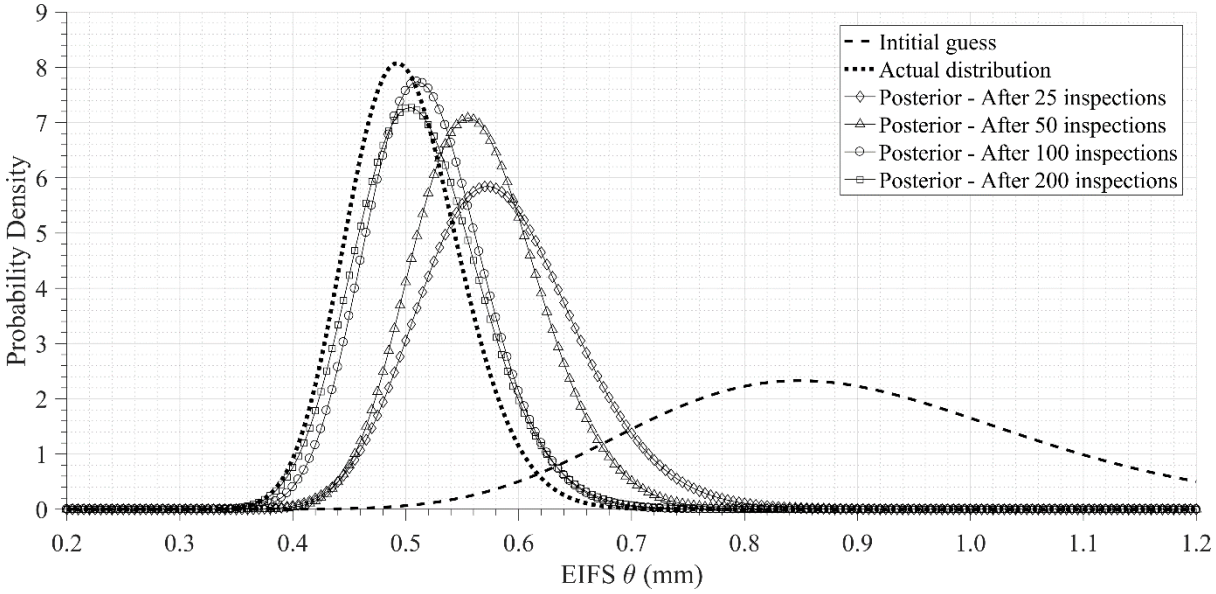

Figure 2.5 here

Figure 2.5. Posterior distributions $f_{\theta|\boldsymbol{D}_i,\boldsymbol{Y}}$ for EIFS after 25, 50, 100, and 200 inspections. The actual EIFSD is shown. The initial guess for the EIFSD is a lognormal distribution with a mean of 0.90 mm and a standard deviation of 0.18 mm. This initial guess for the EIFSD is considered a 'poor' guess since it is far away from the actual EIFSD.

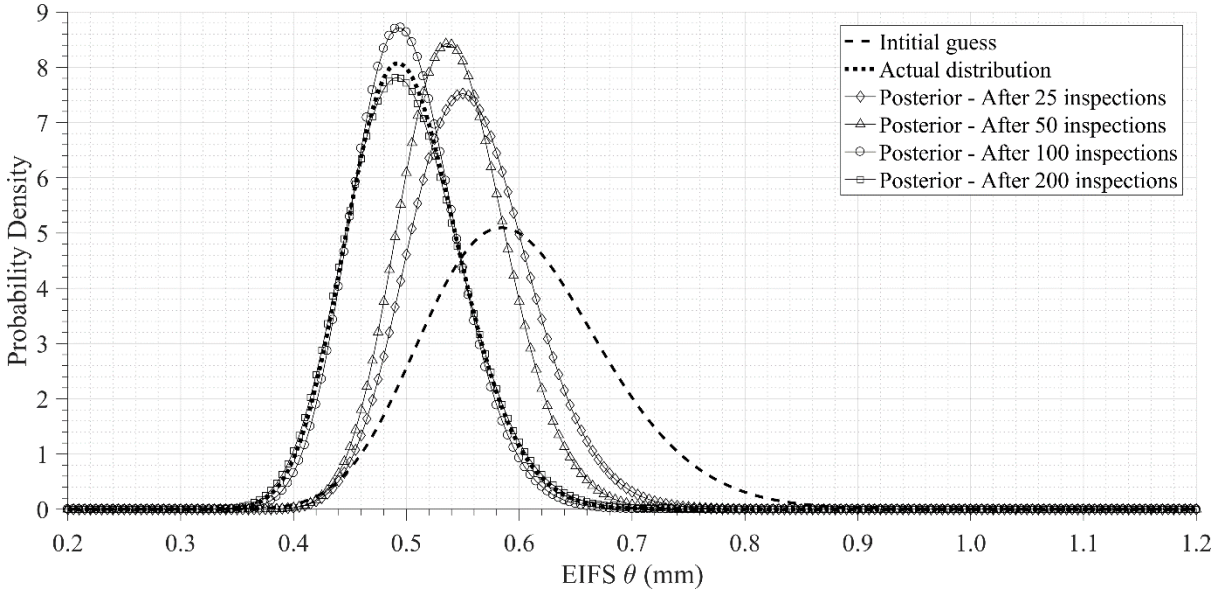

Figure 2.6 here

Figure 2.6. Posterior distributions $f_{\theta|\boldsymbol{D}_i,\boldsymbol{Y}}$ for EIFS after 25, 50, 100, and 200 inspections. The actual EIFSD is shown. The initial guess for the EIFSD is a lognormal distribution with a mean of 0.60 mm and a standard deviation of 0.080 mm. This initial guess for the EIFSD is considered a 'good' guess since it is close to the actual EIFSD.

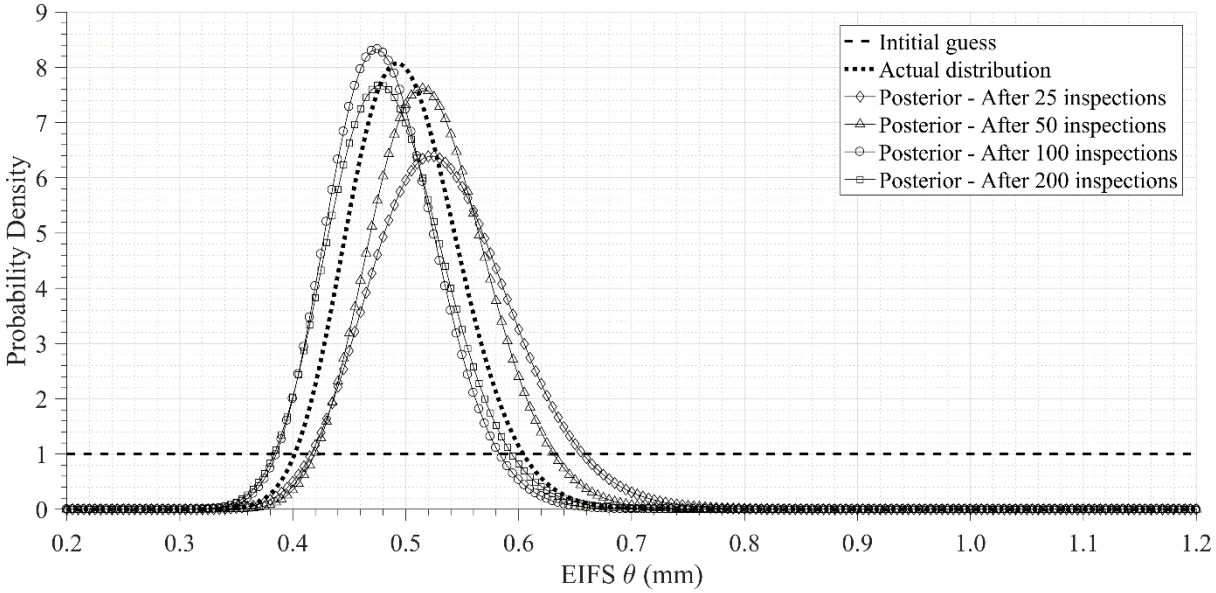

Figure 2.7 here

Figure 2.7. Posterior distributions $f_{\theta|\boldsymbol{D}_i,\boldsymbol{Y}}$ for EIFS after 25, 50, 100, and 200 inspections. The actual EIFSD is shown. The initial guess for the EIFSD is a uniform distribution with a mean of 0.70 mm and a standard deviation of 0.29 mm.

Figure 2.8 (EIFSD_poor.gif) here

Figure 2.8. Animation showing the posterior distributions $f_{\theta|\boldsymbol{D}_i,\boldsymbol{Y}}$ for EIFS after the data from each inspection has been used. The actual EIFSD is shown. The initial guess for the EIFSD is a lognormal distribution with a mean of 0.90 mm and a standard deviation of 0.18 mm. This initial guess for the EIFSD is considered a 'poor' guess since it is far away from the actual EIFSD.

Figure 2.9 (EIFSD_good.gif) here

Figure 2.9. Animation showing the posterior distributions $f_{\theta|\boldsymbol{D}_i,\boldsymbol{Y}}$ for EIFS after the data from each inspection has been used. The actual EIFSD is shown. The initial guess for the EIFSD is a lognormal distribution with a mean of 0.60 mm and a standard deviation of 0.080 mm. This initial guess for the EIFSD is considered a 'good' guess since it is close to the actual EIFSD.

Figure 2.10 (EIFSD_uniform.gif) here

Figure 2.10. Animation showing the posterior distributions $f_{\theta|\boldsymbol{D}_i,\boldsymbol{Y}}$ for EIFS after the data from each inspection has been used. The actual EIFSD is shown. The initial guess for the EIFSD is a uniform distribution with a mean of 0.70 mm and a standard deviation of 0.29 mm.

Table 3. Actual mean of the EIFSD and those predicted from Bayesian updating (BU) after 25, 50, 100, and 200 inspections. Also shown are the initial values. Three different types of initial distribution were investigated.

	Mean μ (mm)					
Type of initial distribution	**Initial value**	**BU 25**	**BU 50**	**BU 100**	**BU 200**	**Actual value**
1) Lognormal (poor guess)	0.90	0.58	0.56	0.52	0.51	0.50
2) Lognormal (good guess)	0.60	0.56	0.54	0.50	0.50	0.50
3) Uniform	0.70	0.53	0.52	0.48	0.49	0.50

Table 3 here

Table 4. Actual standard deviation of the EIFSD and those predicted from Bayesian updating (BU) after 25, 50, 100, and 200 inspections. Also shown are the initial values. Three different types of initial distribution were investigated.

	Standard deviation σ (mm)					
Type of initial distribution	**Initial value**	**BU 25**	**BU 50**	**BU 100**	**BU 200**	**Actual value**
1) Lognormal (poor guess)	0.18	0.070	0.057	0.052	0.056	0.050
2) Lognormal (good guess)	0.080	0.054	0.048	0.046	0.052	0.050
3) Uniform	0.29	0.064	0.053	0.049	0.053	0.050

Table 4 here

2.4. Uses of an Equivalent Initial Flaw Size Distribution

Once a EIFSD f_θ for a particular type of flaw has been found (in this case for edge cracks emanating from fastener holes) it can be used to determine the fatigue life distribution of the structure or to determine the distribution of cracks at a certain time, provided that the structure has similar geometry to the structure that EIFSD was created from, as well as similar loading conditions, and that the same long-crack growth model is used. For a particular combination of cracks, the distribution for the number of cycles required to grow the cracks to some maximum permissible crack size a_p can be estimated using Monte Carlo sampling by considering the uncertainties in the fatigue crack model parameters (represented by $\boldsymbol{Y}$ in this work). This distribution represents the fatigue life of the structure. This procedure can be seen in Figure 2.11.

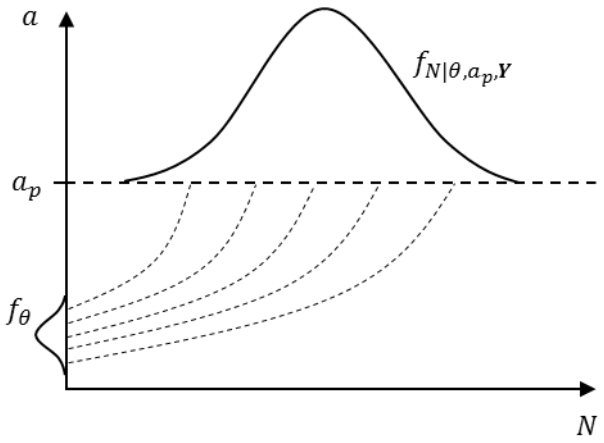

Figure 2.8 here

Figure 2.11. Estimation of the fatigue life distribution of a structure using an EIFSD f_θ.

A distribution for crack size after some number of cycles N_1 can be determined in a similar manner. This is demonstrated in Figure 2.12.

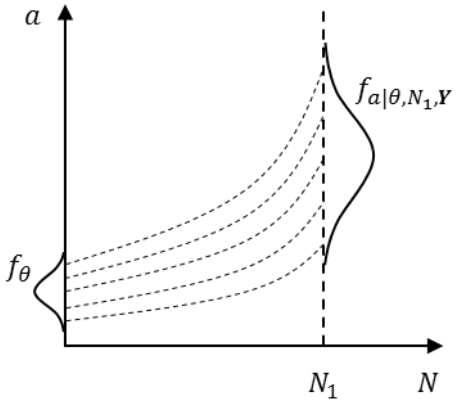

Figure 2.9 here

Figure 2.12 Estimation of the crack size distribution after some number of cycles N_1.

3. Conclusions

In conclusion, a new methodology is presented for the statistical inference of the Equivalent Initial Flaw Size Distribution (EIFSD) for a structure in the presence of Multiple Site Damage (MSD). Bayesian updating is used to update the posterior distributions for the statistical parameters of the EIFSD when new information, in the form of routine inspections, is obtained. An automatic crack extension procedure making use of the Dual Boundary Element Method (DBEM) is used for the efficient analysis of the simultaneous growth of many cracks due to fatigue. Multi-fidelity models, making use of both low-fidelity data and high-fidelity data, are employed via Co-Kriging to act in place of the DBEM model for the Monte Carlo sampling required in the statistical inference of the EIFSD. The application of the proposed methodology is demonstrated for an example featuring a long lap-joint splice commonly found in aircraft fuselages. It was found that the actual EIFSD could be accurately determined with the data from 50 inspections, with both the mean and standard deviation being estimated within about 10% their actual values. If higher quality prior information was available regarding the EIFSD, accurate estimation of the EIFSD could be obtained with the data from a smaller number of inspections. The multi-fidelity models proved to be very effective substitutes for the DBEM model, reducing the total CPU time by a factor of 61,000 while providing an average percentage error of 3.85% when compared to the DBEM model.

Acknowledgements

This research was supported by a grant provided by the Engineering and Physical Sciences Research Council (EPSRC).

References

[1] Findlay SJ, Harrison ND. Why aircraft fail. Materials Today. 2002;5(11):18-25.
[2] Gallagher JP, Giessler FJ, Berens AP, Engle RM. USAF damage tolerant design handbook - Guidelines for the Analysis and Design of Damage Tolerant Aicraft Structures. Wright-Patterson Air Force Base: USAF, 1984.
[3] Forth SC, Everett RA, Newman JA, editors. A Novel Approach to Rotorcraft Damage Tolerance. 6th Joint FAA/DoD/NASA Aging Aircraft Conference; 2002.
[4] Lankford J, Hudak SJ. Relevance of the small crack problem to lifetime prediction in gas turbines. International Journal of Fatigue. 1987;9(2).
[5] Sankararaman S, Ling Y, Mahadevan S. Statistical inference of equivalent initial flaw size with complicated structural geometry and multi-axial variable amplitude loading. International Journal of Fatigue. 2010;32(10):1689-700.
[6] Fawaz SA. Equivalent initial flaw size testing and analysis. Air force research laboratory, Wright-Patterson AFB, 2000 Contract No.: AFRLVA-WP-TR-2000–3024.
[7] Fawaz SA. Equivalent inital flaw size testing and analysis of transport aircraft skin splices. Fatigue & Fracture of Engineering Materials & Structures. 2003.
[8] Moreira PMGP, de Matos PFP, de Castro PMST. Fatigue striation spacing and equivalent initial flaw size in Al 2024-T3 riveted specimens. Theoretical and Applied Fracture Mechanics. 2005;43(1):89-99.
[9] White P, Molent L, Barter S. Interpreting fatigue test results using a probabilistic fracture approach. International Journal of Fatigue. 2005;27(7):752-67.
[10] Molent L, Sun Q, Green AJ. Characterisation of equivalent initial flaw sizes in 7050 aluminium alloy. Fatigue & Fracture of Engineering Materials & Structures. 2006;29(11):916-37.
[11] Johnson WS. The history, logic and uses of the Equivalent Initial Flaw Size approach to total fatigue life prediction. Procedia Engineering. 2010;2(1):47-58.
[12] Kim J, Zi G, Van S, Jeong M, Kong J, Kim M. Fatigue life prediction of multiple site damage based on probabilistic equivalent initial flaw model. Structural Engineering and Mechanics. 2011;38(4):443-57.

[13] Renaud G, Liao M, Bombardier Y. Calculation of Equivalent Initial Flaw Size Distributions for Multiple Site Damage. 55th AIAA Structures, Structural Dynamics, and Materials Conference 2014.
[14] Kim J, Chau-Dinh T, Zi G, Lee WW, Kong JS. Probabilistic fatigue integrity assessment in multiple crack growth analysis associated with equivalent initial flaw and material variability. Engineering Fracture Mechanics. 2016;156:182-96.
[15] Wu Y, Xu Y, Guo X, Bao R. Fatigue life prediction based on equivalent initial flaw size for Al-Li alloy 2297 under spectrum loading. International Journal of Fatigue. 2017;103:39-47.
[16] Alves ASF, Sampayo LMCMV, Correia JAFO, De Jesus AMP, Moreira PMGP, Tavares PJS. Fatigue Life Prediction Based on Crack Growth Analysis Using an Equivalent Initial Flaw Size Model: Application to a Notched Geometry. Procedia Engineering. 2015;114:730-7.
[17] El Haddad M. Prediction of Non Propagating Cracks. Engineering Fracture Mechanics. 1979;11(3):573-84.
[18] Liu Y, Mahadevan S. Probabilistic fatigue life prediction using an equivalent initial flaw size distribution. International Journal of Fatigue. 2009;31(3):476-87.
[19] Xiang Y, Lu Z, Liu Y. Crack growth-based fatigue life prediction using an equivalent initial flaw model. Part I: Uniaxial loading. International Journal of Fatigue. 2010;32(2):341-9.
[20] Lu Z, Xiang Y, Liu Y. Crack growth-based fatigue-life prediction using an equivalent initial flaw model. Part II: Multiaxial loading. International Journal of Fatigue. 2010;32(2):376-81.
[21] Wang Q, Zhang W, Jiang S. Fatigue Life Prediction Based on Crack Closure and Equivalent Initial Flaw Size. Materials (Basel). 2015;8(10):7145-60.
[22] Makeev A, Nikishkov Y, Armanios E. A concept for quantifying equivalent initial flaw size distribution in fracture mechanics based life prediction models. International Journal of Fatigue. 2007;29(1):141-5.
[23] Cross R, Makeev A, Armanios E. Simultaneous uncertainty quantification of fracture mechanics based life prediction model parameters. International Journal of Fatigue. 2007;29(8):1510-5.
[24] Sankararaman S, Ling Y, Shantz C, Mahadevan S. Inference of equivalent initial flaw size under multiple sources of uncertainty. International Journal of Fatigue. 2011;33(2):75-89.
[25] Morse L, Khodaei ZS, Aliabadi MH. Multi-Fidelity Modeling-Based Structural Reliability Analysis with the Boundary Element Method. Journal of Multiscale Modelling. 2017;8(3).
[26] Lefebvre JP, Dompierre B, Robert A, Le Bihan M, Wyart E, Sainvitu C. Failure Probability Assessment using co-Kriging Surrogate Models. Procedia Engineering. 2015;133:622-30.
[27] Straub D, Papaioannou I. Bayesian Updating with Structural Reliability Methods. Journal of Engineering Mechanics. 2014;141(3).
[28] Mallardo V, Sharif Khodaei Z, Aliabadi FMH. A Bayesian Approach for Sensor Optimisation in Impact Identification. Materials (Basel). 2016;9(11).
[29] Huang X, Chen J. Time-Dependent Reliability Model of Deteriorating Structures Based on Stochastic Processes and Bayesian Inference Methods. Journal of Engineering Mechanics. 2015;141(3):04014123.
[30] Portela A, Aliabadi MH. The dual boundary element method- effecitve implementation for crack problems. International Journal for Numerical Methods in Engineering. 1992;33(6):1269-87.
[31] Aliabadi MH. The Boundary Element Method: Applications in solids and structures: John Wiley and Sons; 2002.
[32] Paris PC. The fracture mechanics approach to fatigue. NASA, 1964.
[33] Portela A, Aliabadi MH, Rooke DP. Dual Boundary Element Incremental Analysis of Crack Propagation. Computers and Structures. 1993;46(2):237-47.
[34] Salgado NK, Aliabadi MH. Boundary Element Analysis of Fatigue Crack Propagation in Stiffened Panels. Journal of Aircraft. 1998;35(1):122-30.
[35] Tanaka K. Fatigue Crack Propagation from a Crack Inclined to the Cyclic Tensile Axis. Engineering Fracture Mechanics. 1974;6(3):499-507.
[36] Dowling NE. Mechanical Behavior of Materials: Pearson Education Limited; 2013.
[37] Tuegel EJ, Bell RP, Berens AP, Brussat T, Cardinal JW, Gallagher JP, et al. Aircraft Structural Reliability and Risk Analysis Handbook. Air Force Research Laboratory. Wright-Patterson Air Force Base, 2013 Contract No.: AFRL-RQ-WP-TR-2013-0132.

[38] Burhenne S, Jacob D, Henze GP, editors. Sampling based on Sobol' sequences for Monte Carlo techniques applied to building simulations. 12th Conference of International Building Performance Simulation Assoication; 2011; Sydney.
[39] Viana F, editor Things you wanted to know about the Latin hypercube design and were afraid to ask. 10th World Congress on Structural and Multidisciplinary Optimization; 2013; Orlando, Florida, USA.
[40] Martin JD, Simpson TW. Use of Kriging Models to Approximate Deterministic Computer Models. AIAA Journal. 2005;43(4):853-63.
[41] Keane AJ, Sóbester A, Forrester AIJ. Multi-fidelity optimization via surrogate modelling. Proceedings of the Royal Society A: Mathematical, Physical and Engineering Sciences. 2007;463(2088):3251-69.
[42] Couckuyt I, Dhaene T, Demeester P. ooDACE: A Matlab Kriging Toolbox 2013 [cited 2018]. Available from: http://sumo.intec.ugent.be/ooDACE.
[43] Board NTS. Aircraft Accident Report - Aloha Airlines flight 243. 1988.
[44] Stein ML. Interpolation of Spatial Data: Some Theory for Kriging: Springer-Verlag; 1999.